IOP Publishing Phys. Med. Biol. 65 (2020) 025014 (16pp) https://doi.org/10.1088/1361-6560/ab5b83

Physics in Medicine & Biology

IPEM Institute of Physics and Engineering in Medicine

PAPER

RECEIVED
28 May 2019

REVISED
10 November 2019

ACCEPTED FOR PUBLICATION
25 November 2019

PUBLISHED
16 January 2020

Effects of particle diameter and magnetocrystalline anisotropy on magnetic relaxation and magnetic particle imaging performance of magnetic nanoparticles

Zhiyuan Zhao[1], Nicolas Garraud[2], David P Arnold[2] and Carlos Rinaldi[1,3,4]

[1] Department of Chemical Engineering, University of Florida, Gainesville, FL 32611, United States of America
[2] Department of Electrical and Computer Engineering, University of Florida, Gainesville, FL 32611, United States of America
[3] J. Crayton Pruitt Family Department of Biomedical Engineering, University of Florida, Gainesville, FL 32611, United States of America
[4] Author to whom any correspondence should be addressed.

E-mail: carlos.rinaldi@ufl.edu

Keywords: magnetic nanoparticle, magnetic particle imaging, magnetic relaxation, magnetic anisotropy, Landau–Lifshitz–Gilbert equation

Supplementary material for this article is available online

Abstract

The dynamic magnetization of immobilized spherical single-domain magnetic nanoparticles (MNPs) with uniaxial or cubic magnetocrystalline anisotropy was studied computationally by executing simulations based on the Landau–Lifshitz–Gilbert (LLG) equation. For situations when a static magnetic field was suddenly applied and then removed, the effects of particle diameter and anisotropy (considering both type of symmetry and characteristic energy) on the characteristic magnetic relaxation time were studied parametrically. The results, for both anisotropy symmetries, show that when a static magnetic field is suddenly turned on or off the MNPs undergo a successive two-step or combined one-step relaxation. Whether a MNP relaxes with one or two steps when the field is turned on is determined by the competition between the energy of the applied magnetic field, the magnetic anisotropy energy, and thermal energy. When the applied magnetic field is suddenly turned off, our results show good agreement with theoretical predictions for the cases of $\Delta E_{ani}/k_B T \leqslant 1$ and $\Delta E_{ani}/k_B T \gg 1$, where ΔE_{ani} represents the magnetic anisotropy energy barrier, k_B is the Boltzmann constant and T represents the absolute temperature. For the case of an applied alternating magnetic field (AMF) that is typical of magnetic particle imaging (MPI) applications, the effects of particle diameter and anisotropy symmetry were studied in terms of time-domain magnetization dynamics, dynamic hysteresis loops, harmonic spectra, and x-space point spread functions (PSFs). Results illustrate that the type of magnetocrystalline anisotropy (uniaxial versus cubic) has a significant effect on the MPI performance of the nanoparticles. These computational studies provide insight into the role of particle diameter and magnetic anisotropy on the performance of MNPs for applications in magnetorelaxometry and MPI.

1. Introduction

Over the past decade magnetic nanoparticles (MNPs) have attracted increasing attention for application in magnetic particle imaging (MPI), an emerging biomedical imaging technology that relies on the non-linear dynamic magnetization response of MNPs. In MPI, a static magnetic field gradient is superimposed with a uniform alternating magnetic field (AMF) to generate a small 'field-free region', where the nanoparticles are able to fully respond to the AMF and generate a signal. This signal is then used to reconstruct a quantitative image of the distribution of MNPs in a field of view. While the underlying hardware and physics are similar, there are two approaches of image reconstruction and tracer characterization in common use for MPI: harmonic-space MPI and x-space MPI. In harmonic-space MPI, the response signal due to the MNPs dynamic magnetization is characterized by the harmonic spectrum that is obtained by taking the Fourier transform. In this modality,

good MPI performance is typically indicated by a strong signal of the third harmonic and slow signal decay for increasing harmonics (Eberbeck *et al* 2011, Ludwig *et al* 2012, Weizenecker *et al* 2012). On the other hand, in x-space MPI the MNP signal is represented using a point spread function (PSF) describing the variation of signal intensity with distance from a point source in the imaging volume (Goodwill and Conolly 2010). Compared with harmonic-space MPI, x-space MPI offers the advantages of linearity and shift invariance, real-time imaging, and providing a simple means to estimate MPI tracer resolution from the PSF. Recent work has reported applications of different MPI techniques in tracking nanoparticle accumulation in cancer (Arami *et al* 2017, Yu *et al* 2017a), in evaluating brain injury or gut bleeds (Orendorff *et al* 2017, Yu *et al* 2017b), in quantifying pulmonary drug delivery (Tay *et al* 2018, Wegner *et al* 2018) and in monitoring transplanted stem cells (Nejadnik *et al* 2018) or islets (Wang *et al* 2018).

In order to enhance the performance of MPI technology, prior experimental work (Eberbeck *et al* 2011, Ludwig *et al* 2012, Arami *et al* 2013) has studied the effect of nanoparticle properties on the intensity and resolution of MPI signals. On par with experimental work, previous computational work has also studied the effects of nanoparticle properties on MPI performance, by carrying out simulations based on the Landau–Lifshitz–Gilbert (LLG) equation. For example, Weizenecker *et al* (2012) studied the dependence of MPI signal on particle size and AMF frequency for spherical and prolate ellipsoidal particles, and suggested that smaller anisotropy constants can increase the MPI performance of the particles. However, they assumed that MNPs have uniaxial anisotropy and their easy axes were fixed in the direction of the field. This is typically not the case for spherical MNPs that are used in MPI, such as magnetite nanoparticles, which have cubic magnetic anisotropy and randomly distributed orientations. By using the MNPs and AMFs that are typical in MPI and numerically solving the stochastic differential equation that incorporates the LLG equation, Shah *et al* (2015) studied the magnetic susceptibility and dynamic hysteresis loops of a collection of mobile and immobile spherical magnetite nanoparticles with cubic magnetic anisotropy. Good agreement was observed between computational and experimental results. However, the assumption was made that the orientations of the easy axes of the nanoparticles were partially aligned in the field instead of randomly distributed and the cubic anisotropy of the nanoparticles was finally replaced by an effective uniaxial anisotropy. As such, their algorithm did not actually describe the behavior of particles with cubic anisotropy. Moreover, Shah *et al* (2015) only studied magnetite nanoparticles of specific size and anisotropy constant that were representative of those in their experiments, the results of which cannot be generalized to other particles. By performing simulations of the LLG equation for interacting superparamagnetic iron oxide nanoparticles, some prior work (Them 2017, Wu *et al* 2019) has also demonstrated the effect of magnetic dipole–dipole interactions on the harmonic spectrum of the nanoparticles. But this work is limited to uniaxial anisotropy symmetry and unique nanoparticle and AMF conditions. In summary, in prior work focusing on simulation of MPI performance using the LLG equation has been limited to unique situations or a narrow range of simulation parameters (e.g. particle diameter and magnetic anisotropy constant). Furthermore, none have rigorously modeled cubic magnetic anisotropy nor considered the situation of randomly distributed easy axes of the cubic anisotropy. Additionally, all of the above work focused on calculating the performance of MNPs for harmonic-space MPI. Therefore, while the previous literature has contributed understanding the effect of internal dipole reorientation on MPI performance of nanoparticles, there remains a need for further work to systematically evaluate the effects of different types of magnetocrystalline anisotropy and a wide range of magnetocrystalline anisotropy constant and nanoparticle size on the non-linear dynamic magnetization and MPI performance, especially x-space MPI performance, of spherical particles.

For the case of x-space MPI, the PSF and corresponding resolution of MNPs have been studied by Goodwill and Conolly, using the Langevin function (Goodwill and Conolly 2010). However, the Langevin model assumes that MNPs respond to applied magnetic fields through instantaneous dipole alignment with the field, which is not applicable for nanoparticles that have non-negligible magnetic relaxation time. By considering the relaxation of MNPs through a theoretical magnetization relaxation equation, Croft *et al* (2012) obtained good agreement between their theoretical and experimental results. But the relaxation time is dependent on the equilibrium magnetization of the nanoparticles, which is predicted through the Langevin function and failed to account for particle magnetocrystalline anisotropy. Dhavalikar and Rinaldi (2014) studied both the magnetization harmonics and PSFs for MNPs that relax by the Brownian mechanism, using rotational Brownian dynamics simulations and ferrohydrodynamic magnetization equations. In their work, the nanoparticles were assumed to be 'thermally-blocked' (also known as 'magnetically-blocked') and respond to the changing magnetic field by physical rotation. More recently, Shasha *et al* (2019) reported LLG simulations of performance of suspended magnetite nanoparticles undergoing internal dipole rotation and physical particle rotation and reported values of calculated full-width-at-half-maximum (FWHM) according to an x-space formalism. However, most nanoparticle tracers of interest for MPI are not magnetically blocked or physically rotating, such as would often be the case for nanoparticles that accumulate inside cells. These nanoparticles respond to changes in the magnetic field by only internal magnetic dipole rotation, i.e. through the Néel relaxation mechanism. Moreover, in Shasha and coauthors' work (Shasha *et al* 2019) the magnetite nanoparticles were modeled with uniaxial anisotropy and

the methodology to obtain the x-space MPI performance from the simulations was not described. A review of the recent literature suggests that no prior computational work has studied the effects of different magnetocrystalline anisotropy symmetries, nanoparticle diameter, and anisotropy energy barrier on x-space MPI performance of MNPs undergoing the Néel relaxation.

The most commonly employed approaches to model the magnetization evolution of nanoparticles that respond by the Néel mechanism are based on the stochastic Landau–Lifshitz (LL) equation (Hinzke and Nowak 2002, Berkov *et al* 2006, Usov and Liubimov 2012, Coffey and Kalmykov 2012) or the LLG equation (Shah *et al* 2015, Usadel 2017) that consider large damping of the magnetization field. For examples, Berkov *et al* (2006) applied the LL equation and computational Langevin dynamics simulations to study magnetorelaxometry of MNP suspensions in a range of nanoparticle concentrations, for cases where a static magnetic field was suddenly attenuated or switched off. Leliaert *et al* (2015) developed a macrospin simulation tool based on the LL equation and studied the magnetorelaxometry of uniaxial-anisotropy MNPs with large numbers of particles and for long timescales. By coupling the LLG equation to rotational Brownian simulations, Ilg (2017) studied the effects of size of MNP cluster and value of uniaxial anisotropy constant on magnetorelaxometry of the cluster as a static magnetic field was suddenly switched off. Their results suggest that a fast initial decay due to the Néel relaxation mechanism is followed by long-time relaxation that is due to the Brownian mechanism. However, the above work did not account for the effects of nanoparticle size and different magnetic anisotropy symmetries on magnetorelaxometry, nor provided insight into the dipole dynamics for nanoparticles that are physically fixed in a matrix. Thus, further work is needed to fully understand how nanoparticle properties influence non-linear magnetization dynamics of MNPs.

In this contribution, we report a computational study of the effects of particle diameter and magnetic anisotropy (considering both type of symmetry and barrier energy magnitude) on the magnetization dynamics of immobilized spherical single-domain MNPs in static and AMFs, by employing the LLG equation accounting for the precession of internal magnetic dipoles. In the case of static magnetic fields, a comparison was made between the equilibrium magnetization response of the nanoparticles with uniaxial and cubic anisotropy and the predictions of the Langevin function. Then, we investigated the effects of particle diameter, magnetic anisotropy symmetry and energy on the magnetic relaxation time of the nanoparticles as well as the dynamics of the magnetic dipole moments for cases where a static magnetic field is suddenly turned on and off. For the case of an applied AMF, the intrinsic MPI performance of magnetite nanoparticles that are typical of MPI applications was studied in terms of the evolution and harmonic spectrum of ensemble magnetization, hysteresis loops, and signal PSFs for various nanoparticle sizes. Since the focus of this work is on comparing the magnetization dynamics and MPI performance of MNPs with different sizes and magnetic anisotropies, the effects of magnetic dipole–dipole interactions, and nanoparticle size and anisotropy distributions (Eberbeck *et al* 2011) are left to future studies.

2. Simulation methods

2.1. The Landau–Lifshitz–Gilbert (LLG) equation

The magnetic dipole moment of single-domain MNPs, which have uniform magnetization throughout the nanoparticle volume V_p, is expressed by

$$\mathbf{m} = m_s \hat{\mathbf{m}} = M_d V_p \hat{\mathbf{m}} \tag{1}$$

where m_s represents the magnitude of the magnetic dipole moment, M_d represents the domain magnetization of the particle material, and $\hat{\mathbf{m}}$ is a unit vector specifying the orientation of the magnetic dipole moment. The damped precession of the magnetic dipole moment due to effective fields can be described by the LLG equation (Aharoni 2000)

$$\frac{d\mathbf{m}'}{dt} = -\frac{\gamma_0}{1+\lambda^2}\left[\mathbf{m}' \times \mathbf{B}'_{eff} + \frac{\lambda}{m_s}\mathbf{m}' \times (\mathbf{m}' \times \mathbf{B}'_{eff})\right], \tag{2}$$

where the prime denotes vectors in particle coordinates (as opposed to laboratory coordinates), t represents time, γ_0 is the gyromagnetic ratio, λ is the damping constant, and $\mathbf{B}'_{eff}$ represents the effective field, which contains different energy contributions that are able to provoke changes in the orientation of the magnetic dipole. In our work, we consider the energy contributions of $\mathbf{B}'_{ext}$, due to Zeeman energy (which is generated by the externally applied magnetic field), $\mathbf{B}'_{ani}$, due to magnetocrystalline anisotropy energy, and $\mathbf{B}'_{therm}$, due to thermal agitations. On the right-hand side of equation (2), the first term accounts for the moment precession in the total effective field, whereas the second term accounts for the convergence of this precession trajectory to the direction of the effective field due to the magnetic energy dissipation.

External magnetic fields were applied in the $+z$ direction in laboratory coordinates, represented by $\mathbf{B}_{ext} = B_{dc}\mathbf{i}_z$ with strength B_{dc} for the static magnetic fields and $\mathbf{B}_{ext} = B_{ac}\sin(2\pi ft)\,\mathbf{i}_z$ with amplitude B_{ac} and

frequency f for AMFs, respectively. The magnetic fields can be transformed into the coordinates of nanoparticle i through

$$\mathbf{B}'_{\mathrm{ext},i} = \mathbf{B}_{\mathrm{ext}} \cdot \mathbf{A}_i, \tag{3}$$

where the transformation matrix $\mathbf{A}_i$ is in the form of (Evans (1977))

$$\mathbf{A}_i = \begin{bmatrix} -\zeta^2+\eta^2-\xi^2+\chi^2 & 2(\zeta\chi-\eta\xi) & 2(\zeta\eta+\xi\chi) \\ -2(\eta\xi+\zeta\chi) & -\zeta^2-\eta^2+\xi^2+\chi^2 & 2(\eta\chi-\zeta\xi) \\ 2(\zeta\eta-\xi\chi) & -2(\zeta\xi+\eta\chi) & \zeta^2-\eta^2-\xi^2+\chi^2 \end{bmatrix}. \tag{4}$$

In equation (4), ζ, η, ξ and χ are the quaternion parameters satisfying the condition $\zeta^2+\eta^2+\xi^2+\chi^2 = 1$.

For MNPs with uniaxial anisotropy, the corresponding effective field is in the form of (Robert and Handley (2000))

$$\mathbf{B}'_{\mathrm{ani},i} = 2\frac{K_{\mathrm{u}} V_{\mathrm{p}}}{m_{\mathrm{s}}} \left(\hat{\mathbf{m}}'_i \cdot \hat{\mathbf{u}}'_i\right) \hat{\mathbf{u}}'_i, \tag{5}$$

where K_{u} is the (positive) uniaxial magnetocrystalline anisotropy constant and $\hat{\mathbf{u}}'_i$ is a unit vector that determines the orientation of uniaxial easy axis of nanoparticle i.

For MNPs that have cubic anisotropy, there are two typical easy axis constructions: six easy axes, with orientations along the center of the cubic surface, and eight easy axes, with orientations along the cubic vertices. Since our objective is to predict the MPI performance of magnetite nanoparticles, the eight-easy-axes construction is employed and only the first cubic magnetocrystalline anisotropy constant K_{c} (with negative values) is considered (Robert and Handley 2000). Thus the corresponding effective field is given by (Robert and Handley (2000))

$$\begin{aligned} \mathbf{B}'_{\mathrm{ani},i} = -\frac{2K_{\mathrm{c}} V_{\mathrm{p}}}{m_{\mathrm{s}}} \Big\{ & \left[\left(\hat{\mathbf{m}}'_i \cdot \mathbf{e}'_{2,i}\right)^2 + \left(\hat{\mathbf{m}}'_i \cdot \mathbf{e}'_{3,i}\right)^2\right] \left(\hat{\mathbf{m}}'_i \cdot \mathbf{e}'_{1,i}\right) \mathbf{e}'_{1,i} + \left[\left(\hat{\mathbf{m}}'_i \cdot \mathbf{e}'_{1,i}\right)^2 + \left(\hat{\mathbf{m}}'_i \cdot \mathbf{e}'_{3,i}\right)^2\right] \left(\hat{\mathbf{m}}'_i \cdot \mathbf{e}'_{2,i}\right) \mathbf{e}'_{2,i} \\ & + \left[\left(\hat{\mathbf{m}}'_i \cdot \mathbf{e}'_{1,i}\right)^2 + \left(\hat{\mathbf{m}}'_i \cdot \mathbf{e}'_{2,i}\right)^2\right] \left(\hat{\mathbf{m}}'_i \cdot \mathbf{e}'_{3,i}\right) \mathbf{e}'_{3,i} \Big\}, \end{aligned} \tag{6}$$

where $\mathbf{e}'_i$ is a unit vector that determines three orthogonal directions of nanoparticle i. In equations (5) and (6), the magnitude of $\mathbf{B}'_{\mathrm{ani}}$ indicates the ratio of the total magnetic anisotropy energy barrier ΔE_{ani} to the total magnetic dipole moment m_{s}, both of which are proportional to the particle volume. For the purpose of convenience, we use a unique notation K instead of K_{u} and K_{c}. The height of anisotropy energy barrier ΔE_{ani} is then given by KV_{p} for the uniaxial-anisotropy nanoparticles and $|K|\, V_{\mathrm{p}}/12$ for the eight-easy-axes cubic-anisotropy nanoparticles (Eisenstein and Aharoni 1977a).

By applying the fluctuation–dissipation theorem, the field due to thermal fluctuation $\mathbf{B}'_{\mathrm{therm},i}$ can be characterized by (Brown (1963), Reeves and Weaver (2014))

$$\left\langle \mathbf{B}'_{\mathrm{therm},i}(t) \right\rangle = \mathbf{0}, \tag{7}$$

$$\left\langle \mathbf{B}'_{\mathrm{therm},i}(t)\, \mathbf{B}'_{\mathrm{therm},i}(t+\Delta t) \right\rangle = \frac{2k_{\mathrm{B}} T\lambda}{\gamma_0 m_{\mathrm{s}}} \delta(\Delta t)\, \mathbf{I}, \tag{8}$$

where k_{B} is the Boltzmann constant, T represents the absolute temperature, Δt represents the discrete time interval, the Dirac delta function δ implies the white noise field and $\mathbf{I}$ is the identity matrix.

By introducing the dimensionless variables

$$\upsilon = \frac{k_{\mathrm{B}} T}{\mu_0 m_{\mathrm{s}} M_{\mathrm{d}}}, \tilde{t} = \mu_0 M_{\mathrm{d}} \gamma_0 t, \tilde{f} = \frac{f}{\mu_0 M_{\mathrm{d}} \gamma_0}, \tag{9}$$

and integrating from $\tilde{t}$ to $\tilde{t}+\Delta\tilde{t}$, equation (2) becomes

$$\Delta\hat{\mathbf{m}}' = -\frac{\upsilon}{(1+\lambda^2)} \left[\hat{\mathbf{m}}' \times \left(\alpha \mathbf{e}'_{\mathbf{B}_{\mathrm{ext},i}} + 2\tilde{K}\mathbf{e}'_{\mathbf{B}_{\mathrm{ani},i}} + \sqrt{\frac{2\lambda}{\Delta\tilde{t}}}\mathbf{W}'_i\right) + \lambda\hat{\mathbf{m}}' \times \left(\hat{\mathbf{m}}' \times \left(\alpha \mathbf{e}'_{\mathbf{B}_{\mathrm{ext},i}} + 2\tilde{K}\mathbf{e}'_{\mathbf{B}_{\mathrm{ani},i}} + \sqrt{\frac{2\lambda}{\Delta\tilde{t}}}\mathbf{W}'_i\right)\right)\right] \Delta\tilde{t}, \tag{10}$$

where the Langevin parameter $\alpha = m_{\mathrm{s}} B_{\mathrm{dc}}/k_{\mathrm{B}} T$ and $\mathbf{e}'_{\mathbf{B}_{\mathrm{ext},i}} = \mathbf{i}_z \cdot \mathbf{A}_i$ for the static magnetic fields, $\alpha = m_{\mathrm{s}} B_{\mathrm{ac}}/k_{\mathrm{B}} T$ and $\mathbf{e}'_{\mathbf{B}_{\mathrm{ext},i}} = \sin\left(\tilde{\Omega}\tilde{t}\right) \mathbf{i}_z \cdot \mathbf{A}_i$ for the AMFs, dimensionless angular frequency $\tilde{\Omega} = 2\pi\tilde{f}$, dimensionless anisotropy constant $\tilde{K} = |K|\, V_{\mathrm{p}}/(k_{\mathrm{B}} T)$, $\mathbf{W}'_i$ is a random vector with zero mean and unit standard deviation, $\mathbf{e}'_{\mathbf{B}_{\mathrm{ani},i}} = \left(\hat{\mathbf{m}}'_i \cdot \hat{\mathbf{u}}'_i\right) \hat{\mathbf{u}}'_i$ for the uniaxial anisotropy symmetry, and

$$\begin{aligned} \mathbf{e}'_{\mathbf{B}_{\mathrm{ani},i}} = & \left[\left(\hat{\mathbf{m}}'_i \cdot \mathbf{e}'_{2,i}\right)^2 + \left(\hat{\mathbf{m}}'_i \cdot \mathbf{e}'_{3,i}\right)^2\right] \left(\hat{\mathbf{m}}'_i \cdot \mathbf{e}'_{1,i}\right) \mathbf{e}'_{1,i} \\ & + \left[\left(\hat{\mathbf{m}}'_i \cdot \mathbf{e}'_{1,i}\right)^2 + \left(\hat{\mathbf{m}}'_i \cdot \mathbf{e}'_{3,i}\right)^2\right] \left(\hat{\mathbf{m}}'_i \cdot \mathbf{e}'_{2,i}\right) \mathbf{e}'_{2,i} \\ & + \left[\left(\hat{\mathbf{m}}'_i \cdot \mathbf{e}'_{1,i}\right)^2 + \left(\hat{\mathbf{m}}'_i \cdot \mathbf{e}'_{2,i}\right)^2\right] \left(\hat{\mathbf{m}}'_i \cdot \mathbf{e}'_{3,i}\right) \mathbf{e}'_{3,i}, \end{aligned} \tag{11}$$

for the cubic anisotropy symmetry.

The dimensionless z-direction average magnetization of the nanoparticles is given by

$$\tilde{M}_z = \frac{1}{N}\sum_{i=1}^{N}\frac{m_{z,i}}{m_s}, \tag{12}$$

where $m_{z,i}$ represents the z-direction magnitude of the ith magnetic dipole moment and N is the total number of nanoparticles.

2.2. Simulation parameters and conditions

Simulations were carried out for $N = 3375$ uniform immobilized spherical MNPs ($M_d = 4.46 \times 10^5\ \mathrm{A\,m^{-1}}$) at a temperature of 298.15 K. Since the nanoparticles are motionless and magnetic dipole–dipole interactions are not considered, the nanoparticle number is only significant for calculating the average magnetization of the nanoparticles. Runs were executed starting from random particle configurations using a minimum time interval of $\Delta\tilde{t} = 0.1$ for the case of static magnetic fields. For the dynamics simulations in AMFs using such a small time step would result in prohibitively long simulation time. As such, we compared simulation predictions for various time steps and determined that a time step of $\Delta\tilde{t} = 1$ introduced negligible deviations in predicted response. Thus, the minimum time interval of $\Delta\tilde{t} = 1$ was used for the case of AMFs. For the case of static magnetic fields, we varied the nanoparticle diameter and magnetic anisotropy constant in the range of $5\ \mathrm{nm} \leqslant D_p \leqslant 40\ \mathrm{nm}$ and $3\ \mathrm{kJ\,m^{-3}} \leqslant |K| \leqslant 30\ \mathrm{kJ\,m^{-3}}$, respectively. The intensity of the static magnetic field was varied in the range of $10\ \mathrm{mT} \leqslant B_{dc} \leqslant 200\ \mathrm{mT}$. For the case of AMFs, the particle diameter was varied in the range of $5\ \mathrm{nm} \leqslant D_p \leqslant 50\ \mathrm{nm}$, whereas the anisotropy constant was fixed at $|K| = 13.5\ \mathrm{kJ\,m^{-3}}$ for magnetite nanoparticles (Birks 1950). The AMF amplitude and frequency were 20 mT and 25 kHz, typical of MPI systems in the literature (Gleich and Weizenecker 2005). The value of damping parameter used in the literature is in the range of 0.1 to 1, with larger values corresponding to faster dipole reversal. In the absence of experimental guidance for the appropriate value of the damping parameter we conducted simulations for the values of 0.1 and 1, and compared the results to theoretical predictions of magnetic relaxation. Based on these comparisons, the damping parameter $\lambda = 1$ was used for all simulations presented in the main text. We note that this value has been used in several other studies (Brown 1959, Aharoni 1973, Eisenstein and Aharoni 1977a, Shah *et al* 2015).

2.3. Phenomenological model to analyze results of magnetorelaxometry simulations

In magnetorelaxometry, a collection of immobilized MNPs is subjected to sudden changes of magnitude of an applied static magnetic field, and their dynamic magnetization response is monitored. This situation was modeled using the LLG algorithm described previously by putting the nanoparticles in a zero magnetic field, then applying a static magnetic field of prescribed intensity for a certain time, and finally removing the magnetic field and monitoring relaxation of the nanoparticles towards equilibrium. To interpret the results of these simulations, here we derive simple phenomenological models for the average magnetization of a collection of magnetic dipoles under the assumption that their behavior is characterized by a constant (in time) relaxation time. This simple model should be valid, for example, when the relaxation time of the collection of particles is only a function of the applied magnetic field and the magnetic field is held constant while the average magnetization evolves. We note that the phenomenological models derived here are merely used to justify the way that simulation data (using the full LLG algorithm) are plotted and analyzed below. The evolution of the dimensionless average magnetization can be described by the phenomenological magnetization relaxation equation of Shliomis (1971)

$$\frac{d\tilde{M}_z}{d\tilde{t}} = \frac{1}{\tilde{\tau}}\left(\tilde{M}_z - \tilde{M}_{z,eq}\right), \tag{13}$$

where the dimensionless time $\tilde{\tau} = \mu_0 M_d \gamma_0 \tau$, τ represents the characteristic magnetic relaxation time, and $\tilde{M}_{z,eq}$ represents the dimensionless z-direction average magnetization at equilibrium with the instantaneous magnetic field.

Equation (13) can be solved for the two cases that were modeled to study magnetorelaxometry. For the case where the collection of MNPs is in equilibrium at zero field and then suddenly subjected to a static magnetic field in the $+z$ direction, the solution to the magnetization relaxation equation, in dimensionless form, is

$$\ln\left(1 - \frac{\tilde{M}_z}{\tilde{M}_{z,eq}}\right) = -\frac{\tilde{t}}{\tilde{\tau}}. \tag{14}$$

For the case where the nanoparticles are in equilibrium with an applied magnetic field and the field is suddenly turned off, the solution to the magnetization relaxation equation is given by

$$\ln\left(\frac{\tilde{M}_z}{\tilde{M}_{z,eq}}\right) = -\frac{\tilde{t}}{\tilde{\tau}}. \tag{15}$$

It should be noted that equations (13)–(15) describe an exponential decay of magnetization, in which particles respond to field changes with a constant (in time) relaxation time. In our simulations for the case of magnetorelaxometry the applied magnetic field is either suddenly turned on or suddenly turned off. Hence, when the magnetic field is on the particles are subjected to a constant magnetic field. A simple assumption would be that under such condition particle magnetization evolves with a constant relaxation time and a phenomenological model such as the ones in equations (13)–(15) should capture the dominant behavior and allow for calculation of a relaxation time.

On the other hand, some prior work has also been done to predict the relaxation time of single-domain magnetic particles for various magnetic anisotropy energy and symmetries, by solving the Fokker–Planck differential equation. For example, Aharoni (1973) calculated the field-off relaxation time for MNPs with uniaxial and cubic anisotropy that are under the condition of $\Delta E_{\text{ani}}/k_{\text{B}}T \leqslant 1$

$$\tau_{\text{A1973}} = \frac{M_{\text{d}} V_{\text{p}}}{\gamma_0 k_{\text{B}} T}. \tag{16}$$

For the condition of $\Delta E_{\text{ani}}/k_{\text{B}}T \gg 1$, the field-off relaxation time has also been studied by Brown (1963)

$$\tau_{\text{B1963}} = \frac{M_{\text{d}}}{2K\gamma_0 (KV/\pi k_{\text{B}} T)^{1/2}} \exp\left(\frac{KV_{\text{p}}}{k_{\text{B}} T}\right). \tag{17}$$

for particles with uniaxial anisotropy symmetry, and by Eisenstein and Aharoni (1977b)

$$\tau_{\text{EA1977}} \sim \frac{3\pi M_{\text{d}}}{\sqrt{2}\gamma_0 |K|} \exp\left(\frac{|K| V_{\text{p}}}{12 k_{\text{B}} T}\right). \tag{18}$$

for particles with cubic anisotropy symmetry. It is noted that τ_{A1973}, τ_{B1963} and τ_{EA1977} represent the relaxation times predicted by the models of Aharoni (1973), Brown (1963) and Eisenstein and Aharoni (1977b), respectively, distinguished using the initial of the authors and the year of the publication in the subscript. In our work, we compare simulation results of field-off relaxation time with the predictions of equations (16)–(18), as a means to validate our algorithm.

2.4. Tracer response for MPI

For MPI applications, the performance of MNPs can be assessed using the so-called tracer response (TR), given by Garraud *et al* (2018)

$$TR = \sigma_{\text{Fe}} \dot{\mathcal{F}}\left(H_{\text{app}}\right) = \frac{\dot{M}(t)}{C_{\text{Fe}} \dot{H}_{\text{app}}(t)}, \tag{19}$$

where σ_{Fe} represents the mass magnetization in $A \cdot \text{m}^2/kg_{\text{Fe}}$, $\mathcal{F}$ is a dimensionless function that describes the magnetic behavior of the nanoparticles as a function of H_{app}, H_{app} is the time-dependent applied magnetic field, M represents the magnetization of the nanoparticles, and C_{Fe} represents the iron concentration in $\text{mg}_{\text{Fe}}\,\text{ml}^{-1}$. In equation (19), TR is normalized by the nanoparticle concentration (iron basis) and the rate of change of the magnetic field (which corresponds to the "field-free region" velocity compensation used in x-space MPI reconstruction), and expressed as a function of the applied field instead of time (which accounts for "field-free region" position compensation) (Garraud *et al* 2018).

In our work, $H_{\text{app}} = B_{\text{ac}} \sin(2\pi f t)/\mu_0$ (μ_0 is the vacuum permeability) for the applied z-directed AMF without a static bias magnetic field and $M = n_{\text{p}} m_{\text{s}} \tilde{M}_z$ accounting for the magnetization of the nanoparticles along the field direction. n_{p} represents the number density of MNPs. The signal intensity is then determined from

$$\text{Signal Intensity} = \frac{C_{\text{Fe}} TR}{n_{\text{p}} m_{\text{s}}} = \frac{\dot{M}_z(t)}{\dot{H}_{\text{app}}(t)}, \tag{20}$$

from which the FWHM, deviation between envelope peaks, and peak signal intensity can be obtained. As in the x-space MPI system, the projected intrinsic resolution Δx of a MPI system can be calculated when the constant gradient of static bias field G is known (Garraud *et al* 2018)

$$\Delta x = \frac{\text{FWHM}}{G}. \tag{21}$$

Since in our simulations the minimum time step is too small relative to a cycle of the AMF and thermal agitations are non-negligible, direct numerical differentiation of the magnetization signal results in significant noise. In order to reduce this effect, we applied a moving average of the magnetization signal over a range of p data points. This moving average was only applied when calculating the PSF for a given simulation. Because applying a moving average over too large a time window will remove fast magnetization dynamics generated by the AMF, we sought to determine suitable values of p systematically. To do this, we reasoned that predictions of dynamic

magnetization using the Langevin function would yield the fastest dynamics and determined, for each nanoparticle diameter (since the Langevin function is a function of particle diameter), the largest value of p that would result in no more than 5% deviation in the calculated values of the TR peak magnitude and FWHM with and without moving average. Figure S6 in the supporting material shows the explicit comparisons of results of the Langevin function, including the p value and percent deviation of signal intensity and FWHM, before and after introducing the moving average. One can observe that the moving average hardly influence on the characterizations of the results.

3. Results

3.1. Equilibrium response of magnetization

Figure 1 shows the dimensionless equilibrium average magnetization of a collection of MNPs in a static magnetic field as a function of intensity of the field for anisotropy constant value of $|K| = 13.5\,\mathrm{kJ\,m^{-3}}$, and uniaxial and cubic anisotropy symmetries. In figure 1, $\tilde{M}_{z,\mathrm{eq}}$ refers to the numerical equilibrium magnetization, corresponding to the condition where the slope of the dimensionless z-direction magnetization $\tilde{M}_z$ of the nanoparticles as a function of dimensionless time $\tilde{t}$ is less than 10^{-6}. Accompanied with the scaled anisotropy energy shown in table 1, we observe that in figure 1 the equilibrium magnetization for both anisotropy symmetries have good agreement with the prediction of the Langevin model for $\Delta E_{\mathrm{ani}}/k_{\mathrm{B}}T < 1$. However, for $\Delta E_{\mathrm{ani}}/k_{\mathrm{B}}T > 1$ increasing the value of ΔE_{ani} leads to a divergence of the equilibrium magnetization from the prediction. These results have been shown by prior work (Bean and Livingston 1959), and here give a validation to our algorithms. In addition, figure 1 shows that for the same value of $|K|$, the nanoparticles with uniaxial anisotropy symmetry have a larger divergence of equilibrium magnetization from the Langevin model than those with cubic anisotropy symmetry. This is because the anisotropy energy barrier of the latter nanoparticles is one-twelfth of the anisotropy energy barrier of the former, which results in better alignment of the magnetic dipoles in the field direction and then larger equilibrium average magnetization of the cubic-anisotropy nanoparticles.

3.2. Simulations of magnetorelaxometry

Figure 2 shows representative dimensionless average magnetizations of collections of MNPs as a function of dimensionless time, for nanoparticle diameter $D_{\mathrm{p}} = 15\,\mathrm{nm}$, anisotropy constant value of $|K| = 13.5\ \mathrm{kJ\ m^{-3}}$ ($E_{\mathrm{ani}}/k_{\mathrm{B}}T = 5.80$ for uniaxial symmetry and $E_{\mathrm{ani}}/k_{\mathrm{B}}T = 0.48$ for cubic symmetry) and magnetic field intensity $B_{\mathrm{dc}} = 20\,\mathrm{mT}$ ($\alpha = 3.83$ for both uniaxial and cubic symmetries). The corresponding magnetic relaxation curves were also plotted in terms of equations (14) and (15) for the field-on and off cases, respectively. In the magnetic relaxation curves, the slope is equal to $-1/\tilde{\tau}$. As seen in figure 2, for both types of anisotropy symmetries the average magnetization is zero before a magnetic field is applied. When the external field is suddenly turned on, the magnetization changes to achieve a new equilibrium with the field, through a successive two-step process (characterized by relaxation time τ_1 and τ_2) for the uniaxial-anisotropy nanoparticles and a combined one-step process (characterized by relaxation time τ_{12}) for the cubic-anisotropy nanoparticles. Similarly, when the field is suddenly turned off, the decrease in the magnetization can also occur through two different processes: a successive two-step relaxation (characterized by relaxation time τ_3 and τ_4) and a combined one-step relaxation (characterized by relaxation time τ_{34}) for the uniaxial- and cubic-anisotropy nanoparticles, respectively. Moreover, we observed that in the successive two-step relaxation processes, the first step relaxation was always faster than the second step relaxation, i.e. $\tau_1 < \tau_2$ and $\tau_3 < \tau_4$. Combined with more representative magnetization curves and magnetic relaxation curves shown in figure S1 (stacks.iop.org/PMB/65/025014/mmedia) in the supporting materials, the results suggest that the successive two-step and combined one-step relaxations happen for both MNPs with uniaxial and cubic anisotropy symmetries. More explicitly, we only observed the successive two-step relation when $\Delta E_{\mathrm{ani}} > k_{\mathrm{B}}T$ and $\Delta E_{\mathrm{ani}}/k_{\mathrm{B}}T > \alpha$ for the field-on case and $\Delta E_{\mathrm{ani}} > k_{\mathrm{B}}T$ for the field-off case. Otherwise, the combined one-step relaxation takes place. It should be noted that the two-step relaxation processes observed here is different from that observed by Ilg (2017). In their work the second step was due to Brownian relaxation, whereas in our work the nanoparticles are unable to rotate or translate so that the Brownian relaxation mechanism is abrogated.

To explain the above relaxation behaviors, we focused on the successive two-step process first. When the suddenly applied magnetic field is weak and cannot provide enough energy to overcome the anisotropy energy barrier, the magnetic dipoles which initially align in the easy axes antiparallel to the field direction cannot immediately flip to align with the field. Instead, they instantaneously re-align to some preferable direction nearby the easy axes (corresponding to relaxation step τ_1), and then due to thermal agitations undergo slow flips until an equilibrium state is reached (corresponding to relaxation step τ_2). It is noted that the preferable direction is always located between the directions of the applied field and easy axis that the individual magnetic dipole is initially aligned with. The precise orientation is determined by competition between magnetic field energy and anisotropy barrier energy. When the field is suddenly turned off, since the anisotropy energy is greater than the

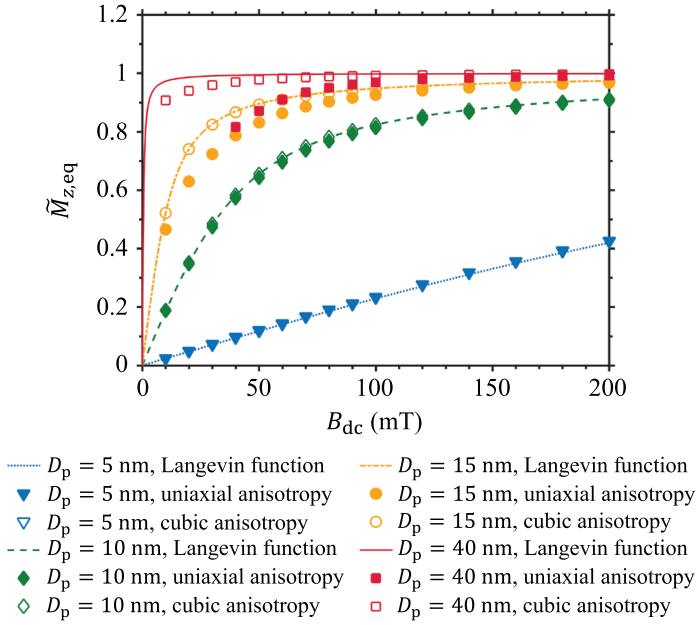

Figure 1. Equilibrium average magnetization of a collection of magnetic nanoparticles in an applied static magnetic field as a function of intensity of the field, for a representative anisotropy constant value of $|K| = 13.5\,\mathrm{kJ\,m^{-3}}$ and various nanoparticle diameters.

Table 1. Scaled anisotropy energy $E_{ani}/k_B T$ for a representative anisotropy constant value of $|K| = 13.5\,\mathrm{kJ\,m^{-3}}$ and various nanoparticle diameters.

D_p, [nm]	5	10	15	40
Uniaxial anisotropy	0.21	1.72	5.80	109.95
Cubic anisotropy	0.02	0.14	0.48	9.16

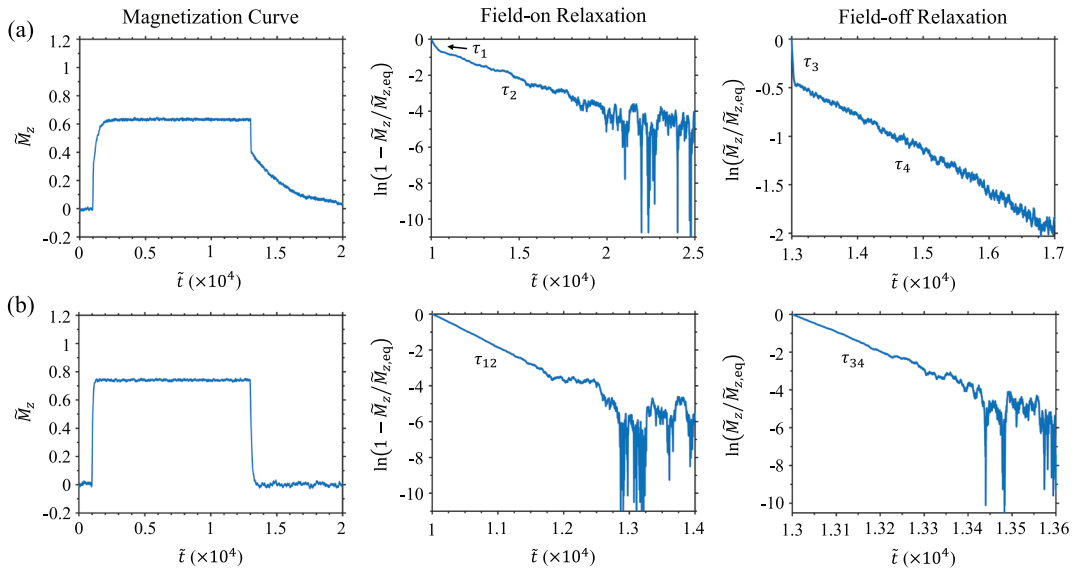

Figure 2. Magnetization curve and corresponding magnetic relaxation curves for collections of immobilized magnetic nanoparticles with (a) uniaxial and (b) cubic anisotropy symmetries, nanoparticle diameter $D_p = 15$ nm, anisotropy constant $|K| = 13.5\,\mathrm{kJ\,m^{-3}}$ ($\Delta E_{ani}/k_B T = 5.80$ for uniaxial symmetry and $\Delta E_{ani}/k_B T = 0.48$ for cubic symmetry), and magnetic field intensity $B_{dc} = 20$ mT ($\alpha = 3.83$ for both uniaxial and cubic symmetries).

thermal energy, magnetic dipoles rapidly snap back to their vicinal easy axes first (corresponding to relaxation step τ_3) and then undergo slow flips until a new equilibrium is achieved (corresponding to relaxation step τ_4). For the combined one-step relaxation, since the anisotropy energy barrier is low, the dipoles that are antiparallel to the field direction can be easily flipped by the suddenly applied field and only experience a one-step relaxation

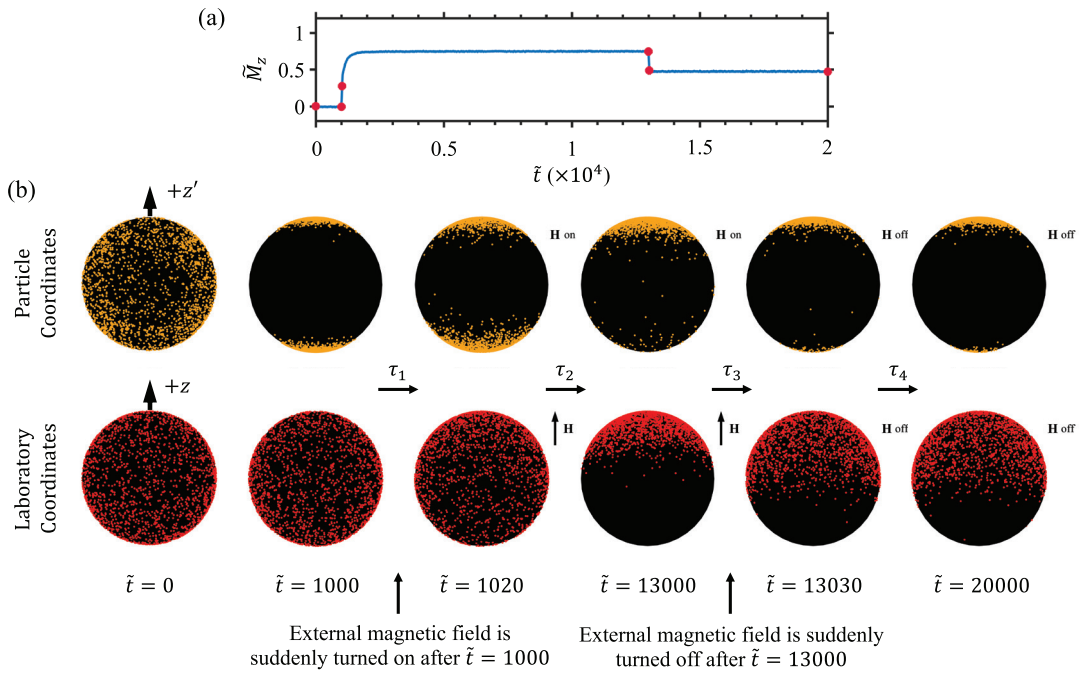

Figure 3. (a) magnetization curve and (b) corresponding representative orientation distributions of magnetic dipoles of a collection of magnetic nanoparticles with uniaxial anisotropy symmetry, for nanoparticle diameter $D_p = 20$ nm and magnetic anisotropy constant $|K| = 13.5$ kJ m^{-3} ($E_{ani}/k_BT = 13.74$) and magnetic field intensity $B_{dc} = 30$ mT ($\alpha = 13.62$). Each yellow/red dot in (b) represents one magnetic dipole moment.

τ_{12}. Similarly, when the field is suddenly turned off, the dominant thermal agitations easily randomize the magnetic dipoles into easy axes with a one-step relaxation time τ_{34}.

Further insight into the successive two-step relaxation process can be obtained from figure 3, which shows magnetization curves and orientation distributions of magnetic dipoles at representative time points, for magnetic field intensity $B_{dc} = 30$ mT ($\alpha = 13.62$) and a collection of uniaxial-anisotropy MNPs with diameter $D_p = 20$ nm and anisotropy constant $|K| = 13.5$ kJ m^{-3} ($E_{ani}/k_BT = 13.74$). It should be noted that in the figure, the $+z'$ direction of the particle coordinates represents the easy axis which points to the particle hemisphere in the $+z$ direction of the laboratory coordinates. The representative time points are also noted in the magnetization curves by red solid circles. In the figure, one can observe that starting from a random configuration and subjected to a zero magnetic field, the magnetic dipoles align in vicinal easy axes ($+z'$ or $-z'$ direction), which acts as a random re-distribution in the laboratory coordinates. When a static magnetic field is suddenly applied in the $+z$ direction, the dipoles slant from the easy axes and align in more preferable directions, through relaxation step τ_1, and then slowly flip to align around the field, through relaxation step τ_2. When the field is suddenly turned off, the magnetic dipoles snap back to the vicinal easy axes, through relaxation step τ_3, and then undergo thermal randomization through relaxation step τ_4. Here relaxation step τ_4 is not obvious because the MNPs are thermally blocked under the simulation conditions. Figure S2 in the supporting material shows the representative orientation distributions of magnetic dipoles for nanoparticles with cubic anisotropy symmetry and under the same condition as in figure 3. Both observations in figures 3 and S2 verify the explanations that we made before for the different relaxation processes of a collection of immobilized MNPs.

We calculated the field-off relaxation times (τ_{34} or τ_3 and τ_4) and plotted them as a function of intensity of the magnetic field for a range of values of magnetic anisotropy constant and types of anisotropy symmetry. The results are shown in figure S3 in the supporting materials. In the figure, some data points are missing because the magnetization of MNPs did not reach equilibrium with the applied field or the nanoparticles are effectively thermally blocked (i.e. with an extremely long relaxation). It is observed that τ_{34} and τ_4 are independent of the field intensity, whereas increasing the field intensity leads τ_3 to decrease first and then plateau. This can be explained because of the small angle between the dipole's preferable direction and the direction of the nearest easy axis under small field intensities. However, for large field intensities ($B_{dc} \geqslant 100$ mT) the anisotropy energy barrier is negligible, which leads to better alignment of the dipoles. Additionally, the field intensity does not affect τ_{34} and τ_4 because of the dominant thermal agitations and irrelevance of initial divergent angle of the magnetic dipole, respectively.

Figure 4 shows the magnetic relaxation time τ_{34}, or τ_3 and τ_4 as a function of dimensionless anisotropy constant $\tilde{K}$ for a range of values of the magnetic anisotropy constant and for the two types of anisotropy

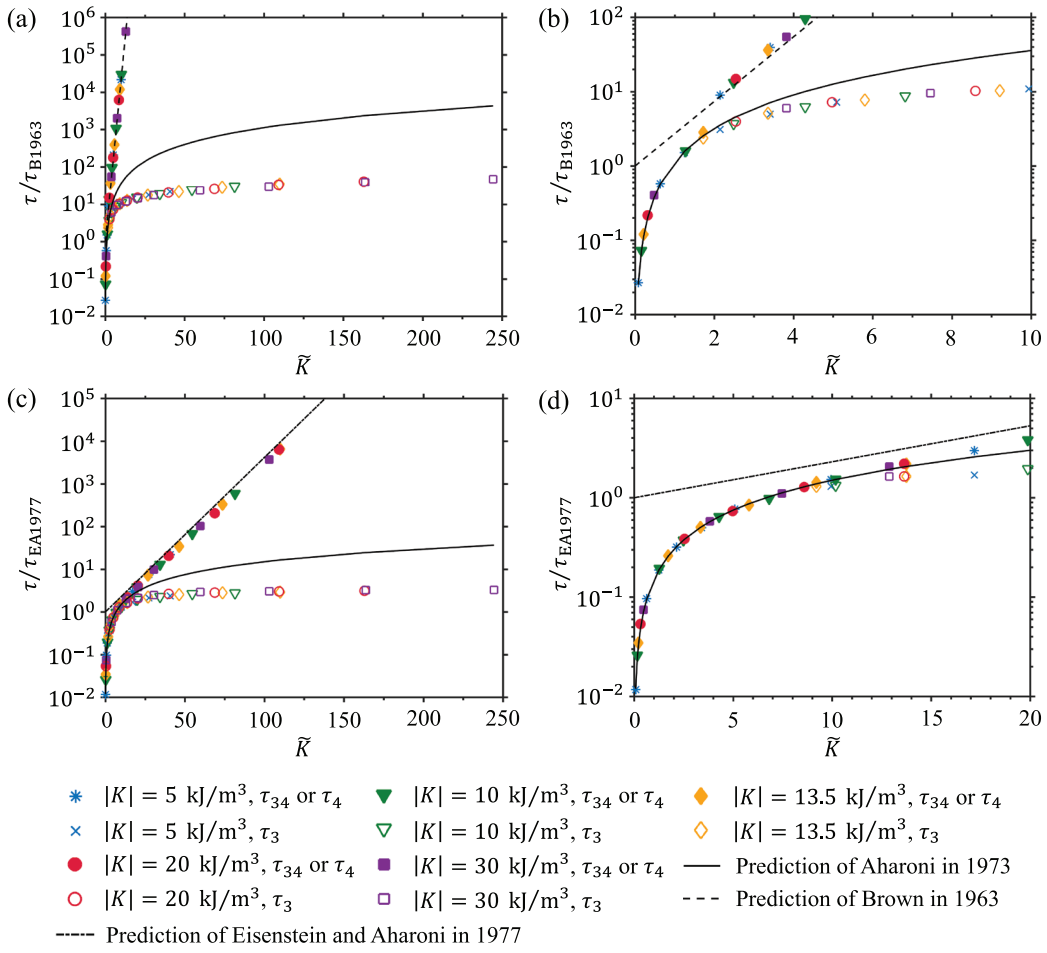

Figure 4. Scaled characteristic magnetic relaxation times τ_{34}, or τ_3 and τ_4 as a function of dimensionless anisotropy constant for various values of the magnetocrystalline anisotropy constant, and for (a) uniaxial- and (c) cubic-anisotropy nanoparticles. (b) and (d) provide zoom-in views for small dimensionless magnetic anisotropy constants in (a) and (c), respectively.

symmetry. It should be noted that in the figure, τ_3 is the average value for cases of $B_{dc} \geqslant 100$ mT. The relaxation times were scaled by τ_{B1963} and τ_{EA1977} for uniaxial- and cubic-anisotropy nanoparticles, respectively. For both types of anisotropy symmetry, one can observe good agreement between the combined one-step relaxation time τ_{34} and the prediction of τ_{A1973} for small values of $\tilde{K}$ (as seen in figures 4(b) and (d)). Increasing the value of $\tilde{K}$ leads to a transition of particle relaxation from the combined one-step process to the successive two-step process, where the scaled τ_3 increases logarithmically and the scaled τ_4 increases linearly. However, the scaled τ_3 is always smaller than the scaled τ_4. For the two types of anisotropy symmetry, figures 4(a) and (c) show that simulation results of τ_3 are in good agreement with the predictions of τ_{B1963} and τ_{EA1977} for the uniaxial- and cubic-anisotropy nanoparticles, respectively. These results serve to validate our algorithms from the perspective of predicting dynamic magnetization response. Here we note that we also carried out simulations using a damping parameter $\lambda = 0.1$ and compared the simulation results to the theoretical predictions of τ_{B1963} and τ_{EA1977}, as shown in figure S5 in the supporting material. As observed in the figure, the relaxation times obtained from simulations using $\lambda = 0.1$ have much poorer agreement with the theoretical predictions. This may be expected since equations (16)–(18) were derived based on the precondition that $\lambda = 1$. We thus believe our use of $\lambda = 1$ is justified. It also should be noted that the successive two-step relaxation processes were not observed by Leliaert *et al* (2015), because they modeled the thermal agitations using the so-called 'stochastic switching', in which the dipole flips as the simulation reaches a pre-specified switching time. As a result, the magnetization curves do not show any thermal fluctuations and the minimum time step is 0.001 s, which is too large to catch the fast first step relaxation.

Figure 5 shows the representative magnetic relaxation time τ_{12} or τ_1 and τ_2 as a function of magnetic field intensity for nanoparticle diameter $D_p = 15$ nm, and a range of values of magnetic anisotropy constant for the two types of symmetry. As seen in the figure, increasing the field intensity leads to a decrease in the relaxation time. Meanwhile, the relaxation of the uniaxial-anisotropy nanoparticles transitions from the successive two-step process to the combined one-step process. The transition field intensity increases with the value of the

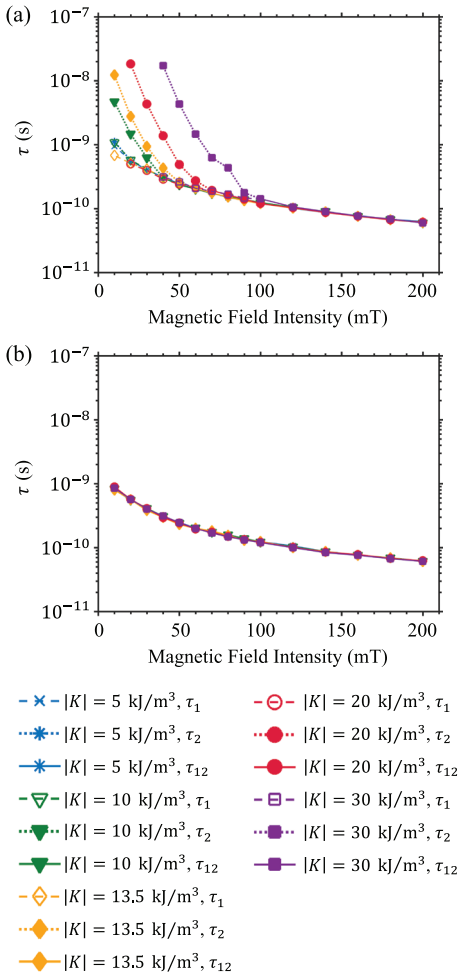

Figure 5. Characteristic magnetic relaxation times τ_{12} or τ_1 and τ_2 as a function of intensity of the applied static magnetic field for nanoparticle diameter $D_p = 15$ nm, various values of anisotropy constant, and (a) uniaxial- and (b) cubic-anisotropy magnetic nanoparticles.

anisotropy constant. This phenomenon is justified because the successive two-step relaxation only happens for the case where the anisotropy energy is dominant over the energy of the magnetic field, and larger transition field intensity is required as the height of the anisotropy energy barrier increases. Our results suggest that the nanoparticles with uniaxial anisotropy symmetry undergo a successive two-step relaxation when $\alpha k_B T/\Delta E_{ani} < 1.34$. However, for nanoparticles with cubic anisotropy symmetry the energy of the magnetic field is always dominant over the anisotropy energy under the conditions studied here, so that only the combined one-step relaxation is observed. In addition, our results suggest that τ_{12} is not a function of the value of the anisotropy constant. This is explained because for the case of combined one-step relaxation the anisotropy energy barrier is too low as compared to other energies (thermal and magnetic). More field-on relaxation times for various particle diameters are shown in figure S4 in the supporting materials, where one can observe that the transition field intensity is also independent of the particle diameter for the case of uniaxial anisotropy symmetry.

3.3. Magnetization signal in an AMF

Figure 6 shows the magnetization curves and corresponding dynamic hysteresis loops of a collection of immobilized magnetite nanoparticles in an AMF typical of MPI, for various particle diameters and anisotropy symmetries. In figures 6(a) and (c), one can observe that increasing the particle diameter results in a change in the shape of the magnetization curve for both uniaxial- and cubic-anisotropy nanoparticles. Simultaneously, a significant response lag with respect to the applied field is observed only for the nanoparticles with uniaxial anisotropy symmetry. The magnetization curve of 40 nm uniaxial-anisotropy nanoparticles has a triangular shape because the anisotropy energy barrier is so high that the magnetic dipoles cannot be flipped by the applied field or thermal agitation. Furthermore, figures 6(b) and (d) show that increasing the particle diameter leads first to a increase and then to a decrease in the area of the dynamic hysteresis loop for the uniaxial-anisotropy nanoparticles, whereas under the conditions studied this is seen to increase monotonically for the cubic-anisotropy nanoparticles. These behaviors are explained because for the same $|K|$ value the uniaxial-anisotropy

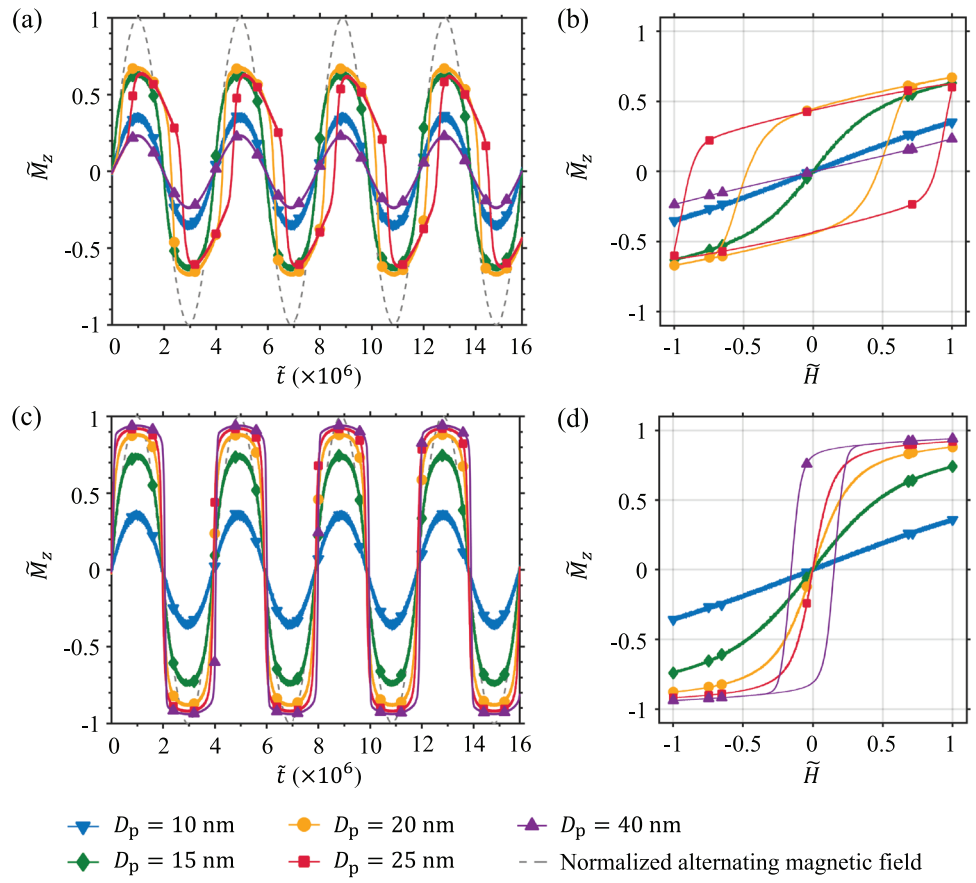

Figure 6. Magnetization curves for collections of magnetite nanoparticles in an alternating magnetic field with amplitude $B_{ac} = 20$ mT and frequency $f = 25$ kHz, for various nanoparticle diameters and for (a) uniaxial and (c) cubic anisotropy symmetries. The corresponding dynamic hysteresis loops are in (b) and (d).

nanoparticles have a higher anisotropy energy barrier so that they experience a longer magnetic relaxation than the cubic-anisotropy nanoparticles.

By taking the fast Fourier transform of the magnetization signals in figures 6 and 7 shows the corresponding harmonic spectra of magnetization for the first 51 harmonics. In the figure, the signals are normalized by the intensity of the first harmonic. It is seen that increasing particle diameter leads the decay rate of signals from the third harmonic to decrease first and then increase for the uniaxial-anisotropy nanoparticles and decrease monotonically for the cubic-anisotropy nanoparticles, under the conditions studied here. According to the analysis method that is typical of harmonic-space MPI, good MPI performance can be determined by the slow decay of harmonic signal from the third harmonic until the plateau of signal amplitude. The plateau above a certain harmonic number is caused by thermal fluctuations which make estimating higher harmonics unreliable. Therefore, our result suggests that for $D_p \geqslant 25$ nm the magnetite nanoparticles that are modeled with cubic anisotropy symmetry have better MPI performance than those modeled with uniaxial anisotropy symmetry. Within the range of particle diameter considered here, the optimal performance for harmonic-space MPI is achieved at $D_p = 20$ nm and $D_p = 40$ nm for the uniaxial- and cubic-anisotropy nanoparticles, respectively.

Figure 8 shows representative PSFs for collections of magnetite nanoparticles in an AMF that is typical for MPI, for nanoparticle diameter $D_p = 20$ nm and the two types of magnetocrystalline anisotropy symmetry. The resolution Δx is calculated for field gradient $G = 5\,\mathrm{T\,m^{-1}}$. As observed in the figure, the signal intensities for uniaxial- and cubic-anisotropy nanoparticles are similar and agree with the prediction of the Langevin model. However, the nanoparticles with uniaxial anisotropy symmetry have smaller FWHM (i.e. finer intrinsic resolution) and larger peak-to-center deviation as compared with the nanoparticles with cubic anisotropy symmetry. Figure 9 shows the corresponding signal intensity, FWHM, and peak deviation for the PSFs calculated for a range of nanoparticle diameters and for the two types of magnetocrystalline anisotropy symmetry. It should be noted that for uniaxial-anisotropy nanoparticles with diameter $D_p \geqslant 25$ nm, the PSF calculation algorithm broke down because the peak shift is beyond the range of applied magnetic field amplitude. As observed in figure 9, for $D_p \leqslant 20$ nm the uniaxial-anisotropy nanoparticles have the same signal intensity, smaller FWHM/expected resolution, and much greater peak deviation as compared to the cubic-anisotropy nanoparticles. For the cubic anisotropy symmetry that magnetite nanoparticles should have, we compared the simulation results with the prediction of

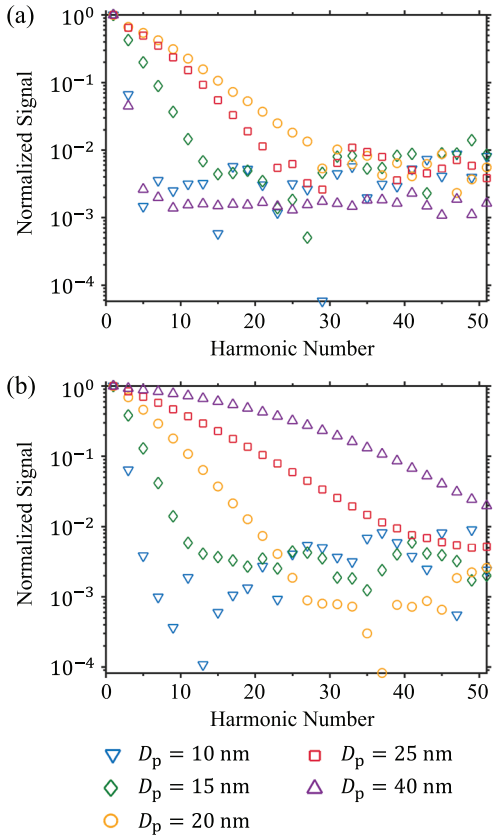

Figure 7. Harmonic spectrum of magnetization signal of a collection of magnetite nanoparticles for alternating magnetic field amplitude $B_{ac} = 20$ mT and frequency $f = 25$ kHz, various nanoparticle diameters, and cases of (a) uniaxial and (b) cubic anisotropy symmetries.

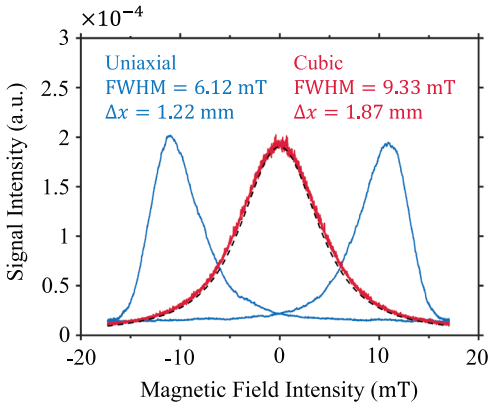

Figure 8. Positive and negative scan tracer response of a collection of magnetite nanoparticles as a function of intensity of applied alternating magnetic field for the field amplitude $B_{ac} = 20$ mT, frequency $f = 25$ kHz, nanoparticle diameter $D_p = 20$ nm, and cases of uniaxial and cubic anisotropy symmetries. In the figure, the corresponding full-width-at-half-maximum (FWHM) and intrinsic resolution of the nanoparticles (Δx) are noted.

the Langevin model and observed good agreement for $D_p \leqslant 30$ nm. For these nanoparticles, increasing the diameter leads to an increase and then slight decrease in signal intensity and a decrease and then slight increase in the FWHM/expected resolution. Both the strongest signal intensity and the smallest FWHM/expected resolution are obtained at $D_p = 35$ nm. Moreover, the peak deviation of the cubic-anisotropy nanoparticles hardly changes with diameter for $D_p \leqslant 30$ nm and slightly increases for $D_p \geqslant 35$ nm. According to the analysis method that is typical of x-space MPI, our results suggest that the optimal performance would be expected for the nanoparticles with $D_p = 35$ nm.

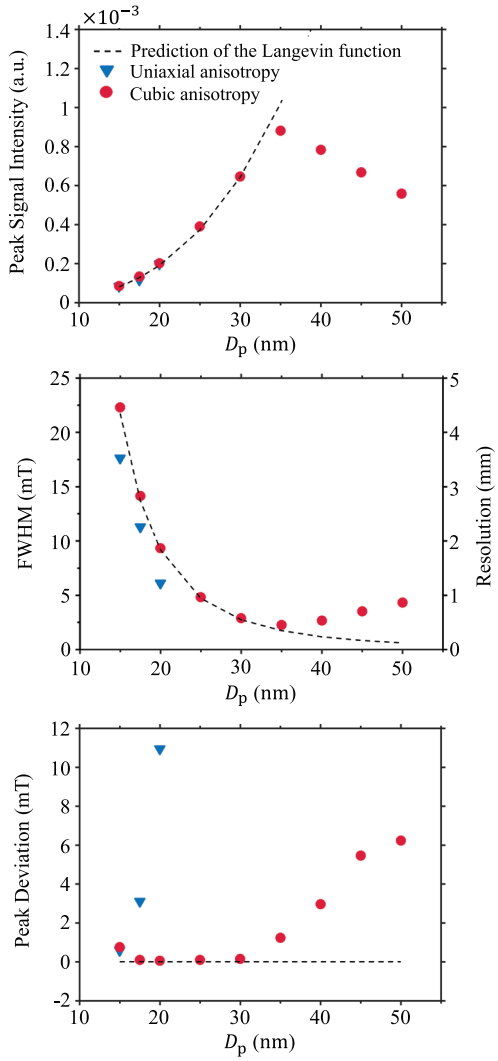

Figure 9. (a) Intensity, (b) full-width-at-half-maximum (FWHM) and (c) peak deviation of magnetization signal of a collection of magnetite nanoparticles as a function of nanoparticle diameter for the field amplitude $B_{ac} = 20$ mT, frequency $f = 25$ kHz, and cases of uniaxial and cubic anisotropy symmetries.

4. Conclusion

We reported a computational study of the effects of particle diameter and magnetocrystalline anisotropy (considering both type of symmetry and barrier energy magnitude) on the magnetization dynamics and MPI performance of a collection of immobilized spherical single-domain MNPs that relax in Néel relaxation mechanism, by carrying out simulations based on the LLG equation. Our LLG simulation algorithm was validated in two ways. First, we demonstrated that for nanoparticles in equilibrium with an applied static magnetic field the average magnetization agreed with the predictions of the Langevin model for $\Delta E_{ani}/k_B T < 1$. Second, we demonstrated that for magnetic dipoles undergoing thermal randomization in the absence of an applied magnetic field the decay in magnetization follows an exponential model with characteristic time in agreement with the predictions of prior works for a wide range of nanoparticle diameters and values of magnetic anisotropy constant, and for uniaxial and cubic anisotropy symmetries.

Our results suggest that for both types of anisotropy symmetry and both cases where a static magnetic field is suddenly turned on and off, MNPs may undergo a successive two-step (periods τ_1 and τ_2 for field turned on, periods τ_3 and τ_4 for field turned off) or combined one-step (period τ_{12} for field turned on and τ_{34} for field turned off) relaxation. Whether a nanoparticle relaxes with one or two periods when the field is turned on is determined by the competition between the energy of the applied magnetic field, the magnetic anisotropy energy, and thermal energy. For the case of an applied AMF that is typical of MPI applications, our work is the first study that compares the effects of uniaxial and cubic magnetocrystalline anisotropies on the x-space MPI performance and resolution of MNPs. The results suggest that different anisotropy symmetries lead to different MPI performance, and this must be taken into consideration when choosing an anisotropy model to describe MNP performance in

MPI. Within the parameters studied, we observed that the optimal x-space MPI performance (signal and resolution) of the cubic-anisotropy magnetite nanoparticles was at $D_p = 35$ nm. In summary, this study provides insight into the roles of nanoparticle diameter and magnetic anisotropy energy and type of symmetry on the nonlinear dynamic magnetization response and performance of MNPs for applications in MPI.

Acknowledgments

This work was supported in part by the US National Science Foundation, Grant CBET-1511113.

Notes

The authors declare no competing financial interest.

ORCID iDs

David P Arnold https://orcid.org/0000-0003-2515-7218

References

Aharoni A 1973 Relaxation-time of superparamagnetic particles with cubic anisotropy *Phys. Rev.* B **7** 1103–7
Aharoni A 2000 *Introduction to the Theory of Ferromagnetism* vol 109 (Oxford: Clarendon)
Arami H, Ferguson R M, Khandhar A P and Krishnan K M 2013 Size-dependent ferrohydrodynamic relaxometry of magnetic particle imaging tracers in different environments *Med. Phys.* **40**
Arami H, Teeman E, Troksa A, Bradshaw H, Saatchi K, Tomitaka A, Gambhir S S, Hafeli U O, Liggitt D and Krishnan K M 2017 Tomographic magnetic particle imaging of cancer targeted nanoparticles *Nanoscale* **9** 18723–30
Bean C and Livingston U D 1959 Superparamagnetism *J. Appl. Phys.* **30** S120–9
Berkov D V, Gorn N L, Schmitz R and Stock D 2006 Langevin dynamic simulations of fast remagnetization processes in ferrofluids with internal magnetic degrees of freedom *J. Phys.: Condens. Matter* **18** S2595–621
Birks J B 1950 The properties of ferromagnetic compounds at centimetre wavelengths *Proc. Phys. Soc.* B **63** 65–74
Brown W F 1963 Thermal fluctuations of a single-domain particle *Phys. Rev.* **130** 1677
Brown W F Jr 1959 Relaxational behavior of fine magnetic particles *J. Appl. Phys.* **30** S130–2
Coffey W T and Kalmykov Y P 2012 Thermal fluctuations of magnetic nanoparticles: fifty years after Brown *J. Appl. Phys.* **112** 121301
Croft L R, Goodwill P W and Conolly S M 2012 Relaxation in x-space magnetic particle imaging *IEEE Trans. Med. Imaging* **31** 2335–42
Dhavalikar R and Rinaldi C 2014 On the effect of finite magnetic relaxation on the magnetic particle imaging performance of magnetic nanoparticles *J. Appl. Phys.* **115** 074308
Eberbeck D, Wiekhorst F, Wagner S and Trahms L 2011 How the size distribution of magnetic nanoparticles determines their magnetic particle imaging performance *Appl. Phys. Lett.* **98** 182502
Eisenstein I and Aharoni A 1977a Asymptotic superparamagnetic time constants for cubic anisotropy. I. Positive anisotropy *Phys. Rev.* B **16** 1278
Eisenstein I and Aharoni A 1977b Asymptotic superparamagnetic time constants for cubic anisotropy. 2. Negative anisotropy constant *Phys. Rev.* B **16** 1285–90
Evans D J 1977 On the representatation of orientation space *Mol. Phys.* **34** 317–25
Garraud N, Dhavalikar R, Unni M, Savliwala S, Rinaldi C and Arnold D P 2018 Benchtop magnetic particle relaxometer for detection, characterization and analysis of magnetic nanoparticles *Phys. Med. Biol.* **63** 175016
Gleich B and Weizenecker R 2005 Tomographic imaging using the nonlinear response of magnetic particles *Nature* **435** 1214–7
Goodwill P W and Conolly S M 2010 The x-space formulation of the magnetic particle imaging process: 1D signal, resolution, bandwidth, SNR, SAR, and magnetostimulation *IEEE Trans. Med. Imaging* **29** 1851–9
Hinzke D and Nowak U 2002 Simulation of magnetization switching in nanoparticle systems *Phys. Status Solidi* a **189** 475–80
Ilg P 2017 Equilibrium magnetization and magnetization relaxation of multicore magnetic nanoparticles *Phys. Rev.* B **95** 214427
Leliaert J, Vansteenkiste A, Coene A, Dupré L and Van Waeyenberge B 2015 Vinamax: a macrospin simulation tool for magnetic nanoparticles *Med. Biol. Eng. Comput.* **53** 309–17
Ludwig F, Wawrzik T, Yoshida T, Gehrke N, Briel A, Eberbeck D and Schilling M 2012 Optimization of magnetic nanoparticles for magnetic particle imaging *IEEE Trans. Magn.* **48** 3780–3
Nejadnik H, Pandit P, Lenkov O, Lahiji A P, Yerneni K and Daldrup-Link H E J M I 2018 Biology, ferumoxytol can be used for quantitative magnetic particle imaging of transplanted stem cells *Mol. Imaging Biol.* **21** 465–72
Orendorff R *et al* 2017 First *in vivo* traumatic brain injury imaging via magnetic particle imaging *Phys. Med. Biol.* **62** 3501–9
Reeves D B and Weaver J B 2014 Nonlinear simulations to optimize magnetic nanoparticle hyperthermia *Appl. Phys. Lett.* **104** 102403
Robert C O and Handley O 2000 *Modern Magnetic Materials: Principles and Applications* (New York: Wiley)
Shah S A, Reeves D B, Ferguson R M, Weaver J B and Krishnan K M 2015 Mixed Brownian alignment and Néel rotations in superparamagnetic iron oxide nanoparticle suspensions driven by an ac field *Phys. Rev.* B **92** 094438
Shasha C, Teeman E and Krishnan K M 2019 Nanoparticle core size optimization for magnetic particle imaging *Biomed. Phys. Eng. Express* **5** 055010
Shliomis M I 1971 Effective viscosity of magnetic suspensions *Zh. Eksp. Teor. Fiz* **61** s1971d
Tay Z W, Chandrasekharan P, Zhou X Y, Yu E, Zheng B and Conolly S 2018 *In vivo* tracking and quantification of inhaled aerosol using magnetic particle imaging towards inhaled therapeutic monitoring *Theranostics* **8** 3676–87
Them K 2017 On magnetic dipole–dipole interactions of nanoparticles in magnetic particle imaging *Phys. Med. Biol.* **62** 5623–39
Usadel K D 2017 Dynamics of magnetic nanoparticles in a viscous fluid driven by rotating magnetic fields *Phys. Rev.* B **95** 104430
Usov N A and Liubimov B Y 2012 Dynamics of magnetic nanoparticle in a viscous liquid: application to magnetic nanoparticle hyperthermia *J. Appl. Phys.* **112** 023901

Wang P et al 2018 Magnetic particle imaging of islet transplantation in the liver and under the kidney capsule in mouse models *Quant. Imagind Med. Surg.* **8** 114

Wegner F, Buzug T M and Barkhausen J 2018 Take a deep breath—monitoring of inhaled nanoparticles with magnetic particle imaging *Theranostics* **8** 3691–2

Weizenecker J, Gleich B, Rahmer J and Borgert J 2012 Micro-magnetic simulation study on the magnetic particle imaging performance of anisotropic mono-domain particles *Phys. Med. Biol.* **57** 7317–27

Wu K, Su D Q, Saha R, Liu J M and Wang J P 2019 Investigating the effect of magnetic dipole–dipole interaction on magnetic particle spectroscopy: implications for magnetic nanoparticle-based bioassays and magnetic particle imaging *J. Phys. D: Appl. Phys.* **52** 335002

Yu E Y *et al* 2017a Magnetic particle imaging for highly sensitive, quantitative, and safe *in vivo* gut bleed detection in a murine model *ACS Nano* **11** 12067–76

Yu E Y, Bishop M I, Zheng B, Ferguson R M, Khandhar A P, Kemp S J, Krishnan K M, Goodwill P W and Conolly S M 2017b Magnetic particle imaging: a novel *in vivo* imaging platform for cancer detection *Nano Lett.* **17** 1648–54